Synthetic Inertia Control of Grid-Connected Inverter Considering the Synchronization Dynamics

Yang Qi, *Member, IEEE*, Han Deng, *Graduate Student Member, IEEE*, Xiong Liu, *Senior Member, IEEE*, and Yi Tang, *Senior Member, IEEE*

***Abstract*—The increasing penetration of renewable energy resources facilitates the carbon footprint reduction process yet reduces the power system inertia. As a result, the grid frequency and the rate of change of frequency (RoCoF) might probably go beyond the normal range, resulting in unexpected load shedding, generator tripping, and even frequency instability. To address this problem, grid-connected inverters are designed to participate in frequency regulation and provide the equivalent inertial support. Nevertheless, the inertia emulation effect is affected by the inverter synchronization dynamic and high RoCoF events may occur as the result of poor synchronization dynamics. In view of this limitation, a synthetic inertia control is developed in this article considering the synchronization dynamics. The synthetic inertia principles and control design guideline are explicitly provided. Finally, hardware experimental results of a scaled-down power system prototype are provided to validate the effectiveness of the proposed approach.**

***Index Terms*—DC–AC inverter, inertia emulation, rate of change of frequency, synchronization.**

I. Introduction

As THE necessary mean of carbon footprint reduction, conventional synchronous generators have been gradually replaced by renewable energy resources (RESs), including photovoltaic, and wind turbines. The grid integration of RES is achieved through grid-connected inverters (GCIs), which normally do not process the inertia property and, therefore, reduce the power system inertia. As a consequence, the grid frequency and the rate of change of frequency (RoCoF) may exceed the normal operation range, resulting in generator tripping, load shedding, and even system blackouts [1], [2]. One recent the 2016 Australia blackout, which affected millions of people and caused a great economic loss. The lack of inertia is believed to be one of the reasons behind this accident [3]. Hence, there is an urgent demand to increase the power system inertia, limit the RoCoF, and ensure the power grid normal operation.

Manuscript received December 4, 2020; revised May 12, 2021 and August 10, 2021; accepted August 19, 2021. Date of publication August 24, 2021; date of current version October 15, 2021. This work was supported by the National Nature Science Foundation of China under Grant 51777169. Recommended for publication by Associate Editor P. Mattavelli. *(Corresponding author: Xiong Liu.)*

Yang Qi is with the Northwestern Polytechnical University, Xi'an 710072, China (e-mail: qiyang@nwpu.edu.cn).

Han Deng and Yi Tang are with the Nanyang Technological University, 639798, Singapore (e-mail: han017@e.ntu.edu.sg; yitang@ntu.edu.sg).

Xiong Liu is with Energy Electricity Research Center, International Energy College, Jinan University, Zhuhai 519070, China (e-mail: liushawn123@ieee.org).

Color versions of one or more figures in this article are available at https://doi.org/10.1109/TPEL.2021.3106948.

Digital Object Identifier 10.1109/TPEL.2021.3106948

To achieve this objective, the concepts of virtual synchronous machines and virtual synchronous generators are invented [4]–[7]. These approaches enable dc–ac inverters to emulate the swing equation of a synchronous generator and provide the equivalent inertia support. It is also found that frequency-droop control can achieve a similar function as long as a first-order low-pass filter is incorporated into the active power control loop [8], [9]. Based on these findings, GCIs can actively contribute to the increase of system inertia. The detailed implementations are well demonstrated in the existing literature [10]–[21].

However, the virtual synchronous generator control as well as frequency droop control would need an energy storage system, e.g., battery, to continuously provide active power in response to a grid frequency deviation. As a result, additional costs, state of charge balancing, and maintenance issues would arise. Since the emulation of inertia only requires temporary active power support, it is possible to achieve this target without large energy storage systems. In [22] and [23], a wind power generation system is controlled to provide the inertia support through releasing the mechanical energy stored in the turbine. However, the speed of turbines should be recovered and this process would influence the inertia emulation effect. In [24] and [25], a dc–ac inverter is connected in series with the noncritical load and virtual inertia is achieved by varying the noncritical load voltage. Despite the effectiveness, extra hardware costs related to the installation of inverter becomes another concern.

From an economic perspective, it is highly expected that inertia support is provided from the existing devices and elements in the power system. Accordingly, the dc capacitors, which are ubiquitously installed in various power-electronics applications, become the promising candidate. In [26], the mapping between dc capacitor voltage and rotor angular speed is formed. Based on that, the inertia support can be provided by proportionally linking the dc capacitor voltage with the power grid frequency [27]. Although the contribution of a single capacitor is limited, the aggregation of all the dc capacitors in a power-electronics-based power system will make a great difference. This concept has been successfully implemented for the modular multilevel converter [28], dc microgrids [29], hybrid ac–dc microgrids [30], and voltage source converter-high voltage direct current (VSC-HVdc) transmission systems [31].

To properly regulate the dc capacitor voltage and synthesize the virtual inertia, various control strategies have been proposed. In [26]–[35], the GCI operates under the current control mode (CCM) and a phase-locked loop (PLL) is utilized for the phase

synchronization and grid frequency measurement. Based on the obtained frequency, the dc voltage reference is determined and maintained by the dc-link voltage controller. Nevertheless, the measured frequency differs from the real grid frequency during the transient. To effectively suppress the RoCoF value at the beginning of a frequency event, the bandwidths of dc voltage controller and PLL should be designed sufficiently high. Yet, the increase of PLL bandwidth will cause stability issues [36]. Moreover, the interactions among different control loops also complicate the analysis and bring a detrimental impact to system stability when the virtual inertia control is performed [37], [38]. As a consequence, additional efforts must be paid to enhance system stability.

An alternative method is to operate the GCI under the voltage control mode (VCM). The basic principle is to generate the GCI frequency reference based on the dc-link voltage. In [39] and [40], the enhanced virtual synchronous machine scheme is developed and the GCI dynamics are well guaranteed through the feedback of grid voltage. Nevertheless, it is difficult to measure the real-time grid voltage if the feeder is long. In comparison, only local measurements are required for the virtual synchronous control [41], the virtual synchronous machine based interface [42], and the matching control [43]. These control strategies successfully make the converter behave like a virtual synchronous machine. As a result, the RoCoF of converter can be improved. However, the RoCoF of power grid is different from the RoCoF of converter during the transient stage. In this sense, the emulated inertia may not necessarily contribute to the grid RoCoF reduction as expected.

Although the inertia emulation principle has been extensively discussed, the impact of GCI synchronization dynamics on the inertia emulation effect was not comprehensively studied. It is this impact that makes the synthetic inertia differ from physical inertia. Moreover, the power system inertial response may even deteriorate if the inertia-emulating GCI is characterized by poor synchronization dynamics. To address this limitation, this article develops a synthetic inertia control that can achieve the desired synchronization dynamics. Consequently, the synthetic inertia of the GCI is in close proximity to physical inertia such that the instant RoCoF value of a frequency event can be effectively reduced. In addition, a step-by-step control parameter design guideline is explicitly provided, which avoids the complications caused by the conventional eigenvalue-analysis approach.

The rest of this article will be organized as follows. Section II discusses the inertia emulation principle and the impacts of GCI synchronization dynamics. Section III introduces the proposed synthetic inertia control and the construction of its architecture. A step-by-step control parameter design guideline is explicitly presented in Section IV. Hardware experimental results of a scaled-down power system prototype are shown in Section V for validation. Finally, Section VI concludes this article.

II. Inertia Emulation Principle

Fig. 1 depicts the schematic diagram of GCI, where $v_{\rm dc}$ is the dc-link voltage v_i is the GCI output voltage, and v_g is the grid voltage. The power system is represented by the synchronous

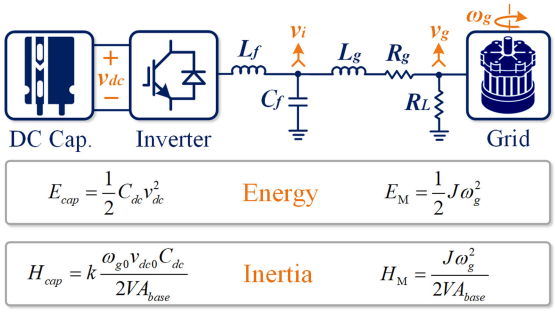

Fig. 1. Analogy between dc capacitors and the synchronous generator.

machine (SM), whose angular speed and the moment of inertia are respectively denoted by ω_g and J. The mechanical energy of the SM rotor is expressed by

$$E_M = \frac{1}{2}J\omega_g^2. \tag{1}$$

Similarly, the electrical energy stored in dc-link capacitors can be expressed as

$$E_{\rm cap} = \frac{1}{2}C_{\rm dc}v_{\rm dc}^2. \tag{2}$$

To increase power system inertia and suppress the frequency deviation, a certain amount of active power support is required during a frequency event. This active power support can either come from the mechanical energy $E_{\rm M}$ or the electrical energy $E_{\rm cap}$. In the connectional power system, SMs are the dominant power generation units. In this case, the power system inertia is mostly determined by the SM rotor. However, the contributions of dc capacitors will significantly increase in the future power-electronic-based power system. The reasons are summarized as follows.

1) As more and more synchronous generators are taken place by power electronic converters, the aggregation of multiple dc capacitors would lead to a large $C_{\rm dc}$ that can store considerable electrical energy.
2) In normal situations, the rotor angular speed ω_g is allowed to vary within 0.4% of nominal value [1]. In other words, only a small portion of $E_{\rm M}$ can be utilized to compensate the power imbalance. In comparison, dc-link voltage $v_{\rm dc}$ can vary within a wider range, e.g., 10%. As a consequence, the utilization rate of $E_{\rm cap}$ would be hundreds of time higher than that of $E_{\rm M}$.

One crucial step for inertia emulation is to proportionally link the dc-link voltage $v_{\rm dc}$ with the grid frequency ω_g, i.e.,

$$v_{\rm dc} = v_{\rm dc0} + k(\omega_g - \omega_{g0}) \tag{3}$$

where $v_{\rm dc0}$ is the nominal dc-link voltage and ω_{g0} is the nominal grid frequency. The proportional gain k is a control-based parameter that determines the synthetic inertia. Meanwhile, the value of k also affects the dc-link voltage deviation and should be carefully designed, as will be discussed in the following section. The per-unit value of the emulated inertia is

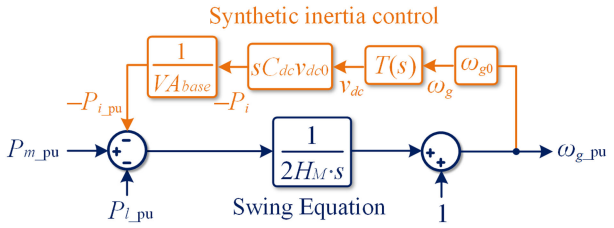

Fig. 2. Schematic diagram of power system frequency control framework.

mathematically defined as

$$\Delta P_{i\_\text{p.u.}} = -2H_{\text{cap}} \frac{d\omega_{g\_\text{p.u.}}}{dt} \tag{4}$$

where $\Delta P_{i\_\text{p.u.}}$ and $\omega_{g\_\text{p.u.}}$ are the per-unit converter active power variation and grid frequency, respectively. From (4), it is clear that

$$\frac{\Delta P_i}{VA_{\text{base}}} = -\frac{2H_{\text{cap}}}{\omega_{g0}} \cdot \frac{d\omega_g}{dt} \tag{5}$$

where VA_{base} is the system base power. According to (3)

$$\frac{dv_{\text{dc}}}{dt} = k \cdot \frac{d\omega_g}{dt}. \tag{6}$$

Meanwhile, ΔP_i results in the change of dc-link voltage v_{dc}. The relationship is given by

$$\Delta P_i = -C_{\text{dc}} v_{\text{dc0}} \cdot \frac{dv_{\text{dc}}}{dt}. \tag{7}$$

From (5) to (7), the term ΔP_i can be eliminated and the emulated inertia H_{cap} is derived as

$$H_{\text{cap}} = k \frac{\omega_{g0} C_{\text{dc}} v_{\text{dc0}}}{2VA_{\text{base}}}. \tag{8}$$

To investigate the impact of synthetic inertia H_{cap} on the grid RoCoF, Fig. 2 illustrate the simplified schematic diagram of the power system frequency regulation framework. Recalling the synchronous generator swing equation

$$P_{m\_p.u.} - P_{l\_p.u.} = 2H_M \cdot \frac{d\omega_{g\_p.u.}}{dt} \tag{9}$$

where $P_{l\_\text{p.u.}}$ is the active power consumed by the load and $P_{m\_\text{p.u.}}$ is the mechanical input power of the SM. If there is a mismatch between $P_{l\_\text{p.u.}}$ and $P_{m\_\text{p.u.}}$, the RoCoF value will deviate from zero. If the synthetic inertia control is not implemented, the transfer function from $P_{l\_\text{p.u.}}$ to $\omega_{g\_\text{p.u.}}$ is given by

$$\frac{\hat{\omega}_{g\_p.u.}(s)}{\hat{P}_{l\_p.u.}(s)} = \frac{-1}{2H_M s}. \tag{10}$$

Based on the initial value theorem, the initial RoCoF after a step change $\Delta P_{l\_\text{p.u.}}$ equals

$$\left.\frac{d\omega_{g\_p.u.}}{dt}\right|_{t=0} = \lim_{s\to\infty}\left(\frac{-s}{2H_M s} \cdot s \cdot \frac{\Delta P_{l\_p.u.}}{s}\right) = \frac{-\Delta P_{l\_p.u.}}{2H_M}. \tag{11}$$

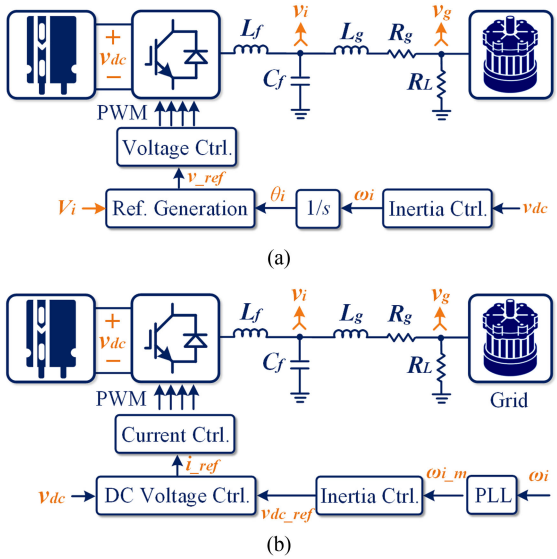

Fig. 3. Synthetic inertia control block diagrams. (a) GCI under the voltage control mode. (b) GCI under the current control mode.

When the synthetic inertia control is implemented and $T(s)$ is ideally designed as the proportional gain k, i.e.,

$$T(s) = \frac{\hat{v}_{\text{dc}}(s)}{\hat{\omega}_g(s)} = k. \tag{12}$$

The transfer function from $P_{l\_\text{p.u.}}$ to $\omega_{g\_\text{p.u.}}$ then becomes

$$\frac{\hat{\omega}_{g\_p.u.}(s)}{\hat{P}_{l\_p.u.}(s)} = \frac{-1}{\left(2H_M + \frac{\omega_{g0} k C_{\text{dc}} v_{\text{dc0}}}{VA_{\text{base}}}\right) s} = \frac{-1}{2(H_M + H_{\text{cap}})s} \tag{13}$$

which means the power system inertia is enlarged to $H_{\text{M}} + H_{\text{cap}}$. Similarly, the inertia RoCoF is reduced to $-\Delta P_{l\_\text{p.u.}}/2(H_{\text{M}} + H_{\text{cap}})$.

This objective is achieved through the proper control of GCI. Generally, the control strategies can be classified into two types and the principles are illustrated in Fig. 3.

Fig. 3(a) illustrates the VCM, where ω_i is the GCI frequency, V_i is the GCI voltage magnitude, and v_{ref} is the reference voltage. Based on the value of v_{dc}, a synthetic inertia controller regulates the GCI frequency ω_i. Nevertheless, even if ω_i is proportionally linked with v_{dc}, the objective of (3) cannot be precisely realized.

This is due to the fact ω_i does not equal ω_g during the transient stage. In other words, the synchronization dynamics between ω_i and ω_g would make the GCI synthetic inertia different from the physical inertia.

Fig. 3(b) illustrates the CCM, where the GCI is controlled as a current source. A PLL is utilized to obtain the phase angle and frequency information. Based on the measured frequency ω_{i_m}, a synthetic inertia controller regulates the dc-link voltage reference $v_{\text{dc\_ref}}$. Meanwhile, a dc voltage controller is employed to track $v_{\text{dc\_ref}}$ and generate the reference current i_{ref}. Similarly, the measured frequency ω_{i_m} does not equal ω_g during the transient stage so that the synchronization dynamics are coupled with the inertia emulation effect. Moreover, the dynamics of dc voltage controller introduce an additional delay between $v_{\text{dc\_ref}}$

and $v_{\rm dc}$. As a result, the inertia emulation effect may be further affected.

In summary, the actual transfer function $T(s)$ is a frequency-domain transfer function rather than a proportional gain

$$T(s) = \frac{\hat{v}_{\rm dc}(s)}{\hat{\omega}_g(s)} \neq k. \tag{14}$$

The superscript ^ represents the perturbation of variables. It should be mentioned that the poles of $T(s)$ will greatly affect the inertia emulation effect and RoCoF of a frequency event. When the dynamic response of $T(s)$ is sluggish, the electrical energy stored in the dc capacitors cannot be immediately released to compensate the instantaneous power mismatch. As a result, the initial RoCoF of a frequency event cannot be reduced. Hence, it is expected that the dc-link voltage and the synchronization dynamic performance are fast and stable such that the GCI can effectively contribute to the power system inertial response.

III. Modeling and Control Architecture Design

To fulfill the inertia emulation expectation, it is necessary to construct a small-signal model, derive the transfer function $T(s)$, and eventually select a proper control architecture. In this article, the VCM shown in Fig. 3(a) is considered, since it avoids the use of PLL and performs better under weak grid scenarios.

A. Small-Signal Modeling

Without loss of generality, a linear controller $G_{AL}(s)$ is employed as the inertia controller in Fig. 3(a). The transfer function of $G_{AL}(s)$ is given by

$$G_{AL}(s) = \frac{\hat{\omega}_i(s)}{\hat{v}_{\rm dc}(s)} = \frac{a_0 + a_1 s + a_2 s^2 + \dots}{1 + b_1 s + b_2 s^2 + \dots} \tag{15}$$

where a_0, a_1, $a_2 \dots$, b_1, b_2, $\dots$ are the constants to be determined. Equation (15) forms the GCI active power control loop and provides the reference frequency ω_i. Meanwhile, the GCI voltage magnitude V_i is calculated based on Q–V droop control, as the convention of most VCMs

$$V_i = V_0 - k_q(Q_i - Q_0) \tag{16}$$

where k_q is the reactive power droop gain, and V_0 and Q_0 are the nominal voltage and reactive power, respectively. Suppose that the GCI voltage leads grid voltage by δ, the active and reactive power of GCI can be expressed as

$$P_i = \frac{V_i V_g \omega_0 L_g}{2(\omega_0^2 L_g^2 + R_g^2)} \sin\delta + \frac{V_i(V_i - V_g\cos\delta)R_g}{2(\omega_0^2 L_g^2 + R_g^2)} \tag{17}$$

$$Q_i = -\frac{V_i V_g R_g}{2(\omega_0^2 L_g^2 + R_g^2)} \sin\delta + \frac{V_i(V_i - V_g\cos\delta)\omega_0 L_g}{2(\omega_0^2 L_g^2 + R_g^2)}. \tag{18}$$

Based on [44], the linearization of (17) and (18) at the equilibrium point is expressed as

$$\begin{cases} \hat{P}_i(s) = G_{\delta P}\cdot\hat{\delta}(s) + G_{VP}\cdot\hat{V}_i(s) \\ \hat{Q}_i(s) = G_{\delta Q}\cdot\hat{\delta}(s) + G_{VQ}\cdot\hat{V}_i(s) \end{cases} \tag{19}$$

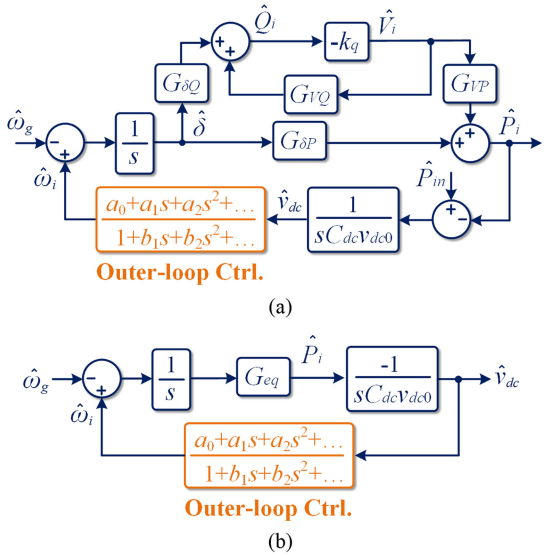

Fig. 4. System small-signal model. (a) Representation. (b) Simplification.

where the coefficients $G_{\delta P}$, G_{VP}, $G_{\delta Q}$, and G_{VP} equal

$$\begin{cases} G_{\delta P} = \frac{V_i V_g(\cos\delta_0\omega_0 L_g + \sin\delta_0 R_g)}{2(\omega_0^2 L_g^2 + R_g^2)} \\ G_{VP} = \frac{V_g\sin\delta_0\omega_0 L_g + (2V_i - V_g\cos\delta_0)R_g}{2(\omega_0^2 L_g^2 + R_g^2)} \\ G_{\delta Q} = \frac{V_i V_g(\sin\delta_0\omega_0 L_g - \cos\delta_0 R_g)}{2(\omega_0^2 L_g^2 + R_g^2)} \\ G_{VQ} = \frac{-V_g\sin\delta_0 R_g + (2V_i - V_g\cos\delta_0)X_g}{2(\omega_0^2 L_g^2 + R_g^2)}. \end{cases} \tag{20}$$

The dc capacitor voltage is determined by

$$P_{in} - P_i = \frac{d}{dt}\left(\frac{1}{2}C_{\rm dc}v_{\rm dc}^2\right) \tag{21}$$

where P_{in} is the input power of the dc capacitor. From (21)

$$\hat{P}_{in}(s) - \hat{P}_i(s) = sC_{\rm dc}v_{\rm dc0}\cdot\hat{v}_{\rm dc}(s). \tag{22}$$

According to (20) and (22), the system small-signal model is built and displayed in Fig. 4(a). To derive the transfer function from $\omega_g(s)$ to $v_{\rm dc}(s)$, Fig. 4(a) is equivalently transferred into Fig. 4(b) and the gain G_{eq} equals

$$G_{eq} = G_{\delta P} - \frac{G_{\delta Q}G_{VP}k_q}{1 + k_q G_{VQ}}. \tag{23}$$

From Fig. 4(b), it is clear that the transfer function $T(s)$ can be derived as

$$T(s) = \frac{\hat{v}_{\rm dc}(s)}{\hat{\omega}_g(s)} = \frac{G_{eq}}{C_{\rm dc}v_{\rm dc0}s^2 + G_{eq}G_{AL}(s)}. \tag{24}$$

B. Reshaping Synchronization Dynamics

In this article, the architecture of $G_{AL}(s)$ is inversely designed in order to achieve the desired dynamic performance. Recalling the typical transfer function of a second-order system

$$\phi(s) = \frac{A_0}{s^2 + 2\xi\omega_r s + \omega_r^2} \tag{25}$$

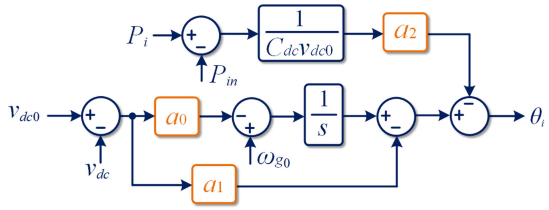

Fig. 5. Block diagram of the active power control loop.

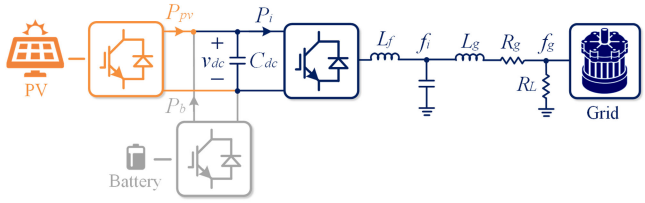

Fig. 6. Circuit diagram when additional power sources are coupled to dc link.

where ξ is the damping ratio and ω_r is the resonant frequency. By comparing (24) with (25), the general architecture of $G_{AL}(s)$ can be inversely determined as

$$G_{AL}(s) = \frac{\hat{\omega}_i(s)}{\hat{v}_{\rm dc}(s)} = a_0 + a_1 \cdot s + a_2 \cdot s^2. \tag{26}$$

Equation (26) includes a proportional term and two differential terms. Due to noise amplification concerns, differential operations can hardly be implemented in the digital controller. To avoid using differential operations, (26) can be alternatively expressed as

$$\hat{\theta}_i(s) = \frac{\hat{\omega}_i(s)}{s} = a_0\frac{\hat{v}_{\rm dc}(s)}{s} + a_1\hat{v}_{\rm dc}(s) + a_2\frac{\hat{P}_{in}(s) - \hat{P}_i(s)}{C_{\rm dc}v_{\rm dc0}}. \tag{27}$$

The corresponding control block diagram of (27) is displayed in Fig. 5. An alternative way to approximate (26) is adding two high-frequency poles in the denominator of $G_{AL}(s)$. The corner frequency should be well beyond the voltage control bandwidth. Meanwhile, the corner frequency cannot be set too high due to the high-frequency noise amplification concern.

IV. Control Parameter Design

This section aims to provide an explicit guideline for control parameters. A step-by-step procedure will be presented, starting from the outer-loop controller to the inner-loop controller.

A. Design of the Inertia Constant

Taking (26) into (24), the transfer function $T(s)$ is given by

$$T(s) = \frac{1}{\left(\frac{C_{\rm dc}v_{\rm dc0}}{G_{eq}} + a_2\right)s^2 + a_1 \cdot s + a_0}. \tag{28}$$

The steady-state gain of $T(s)$ is calculated as

$$T(s)|_{s=0} = a_0^{-1}. \tag{29}$$

The constant a_0, which equals the inverse of constant k in (3), is determined as

$$a_0 = \frac{1}{k} = \frac{\Delta\omega_{g\_\max}}{\Delta v_{\rm dc\_max}} \tag{30}$$

where $\Delta\omega_{g\_\max}$ denotes the maximum grid frequency deviation. The typical value of $\Delta\omega_{g\_\max}$ is 0.4π rad/s. $\Delta v_{\rm dc\_max}$ refers to the maximum dc voltage deviation. To avoid overmodulation, it is required that

$$\Delta v_{\rm dc\_max} < (1-m)v_{\rm dc0} \tag{31}$$

where m is the SPWM modulation index. In this case

$$k < \frac{(1-m)v_{\rm dc0}}{\Delta\omega_{g\_\max}}. \tag{32}$$

Meanwhile, the converter output power reaches a peak value right after a power system load change $\Delta P_{l\_\rm p.u}$. The peak power can be calculated according to Fig. 2

$$\begin{aligned} P_{\max} &= \lim_{s\to\infty}\left(\frac{sP_i(s)}{P_{l\_p.u.}(s)}\cdot\frac{\Delta P_{l\_p.u.}}{s}\right) \\ &\approx \frac{C_{\rm dc}v_{\rm dc0}k\omega_{g0}\Delta P_{l\_p.u.}}{2H_M V A_{\rm base} + C_{\rm dc}v_{\rm dc0}k\omega_{g0}}. \end{aligned} \tag{33}$$

The selection of the constant a_0, i.e., $1/k$, should also consider the power rating of converter and ensure that the converter will not be overloaded and also the junction temperature limit of the converter

To achieve the expected synthetic inertia H_0, the capacitance requirement is expressed as

$$C_{\rm dc} = \frac{2H_0 V A_{\rm base}}{k\omega_{g0}v_{\rm dc0}}. \tag{34}$$

When H_0 is considerable, a large aggregated dc capacitance is required and the existing dc capacitors in a power grid may not satisfy this requirement. Fortunately, the additional power sources coupled to the dc-link can reduce the capacitance need, as shown in Fig. 6.

For the PV converter, the power reserve control proposed in [45] and [46] makes it possible to provide the inertia support from the PV module. The PV output power variation is given by

$$P_{\rm pv}(s) = -\frac{2VA_{\rm base}H_{\rm pv}}{\omega_{g0}}s\cdot\omega_g(s) \tag{35}$$

where $H_{\rm pv}$ is the per-unit inertia contributed by the PV.

For the battery, the frequency-derivative control proposed in [47] can achieve the similar function, as shown by

$$P_b(s) = -\frac{2VA_{\rm base}H_b}{\omega_{g0}}s\cdot\omega_g(s) \tag{36}$$

where $H_{\rm pv}$ is the per-unit inertia contributed by battery modules. The dc-link voltage dynamics are reformulated as

$$P_b(s) + P_{\rm pv}(s) - P_i(s) = sC_{\rm dc}v_{\rm dc0}\cdot v_{\rm dc}(s). \tag{37}$$

Combining (6) and (35)–(37), it can be obtained that

$$P_i(s) = -\frac{2VA_{\rm base}(H_{\rm pv}+H_b+H_{\rm cap})}{\omega_{g0}}s\cdot\omega_g(s). \tag{38}$$

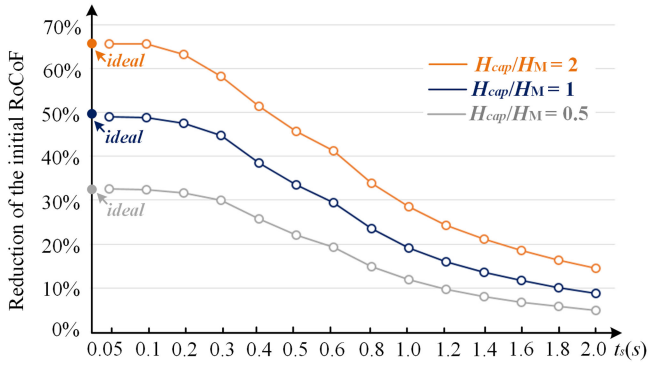

Fig. 7. Reduction of the maximum RoCoF with different settling time t_s.

Equation (38) indicates that the total equivalent inertia is the sum of $H_{\rm pv}$, H_b, and $H_{\rm cap}$. Benefited from this, the requirement of dc capacitance is reduced as

$$C_{\rm dc} = \frac{2(H_0 - H_b - H_{\rm pv})VA_{\rm base}}{k\omega_{g0}v_{\rm dc0}}. \tag{39}$$

Although the proper utilization of renewable energy resources can reduce the dc capacitance requirement. The corresponding implementation is not the main focus of this article. Therefore, the worst case is considered in this article and $H_{\rm pv} = H_b = 0$.

B. Design of Settling Time and Damping Ratio

Next, the resonant frequency ω_r and damping ratio ξ of (28) are calculated as

$$\omega_r = \left(\frac{G_{eq}a_0}{C_{\rm dc}v_{\rm dc0} + G_{eq}a_2}\right)^{1/2} \tag{40}$$

$$\xi = \frac{a_1}{2}\left(\frac{G_{eq}}{a_0C_{\rm dc}v_{\rm dc0} + a_2a_0G_{eq}}\right)^{1/2}. \tag{41}$$

To avoid an undesired oscillation and undershoot, the critical damping scenario $\xi = 1$ is pursued. In this case, the settling time t_s when the value of $v_{\rm dc}(t)$ reach and steady within 5% of its final value can be approximated as

$$t_s = \frac{4.75}{\omega_r}. \tag{42}$$

The settling time t_s plays a crucial role in limiting the initial RoCoF of a frequency event and should be properly selected to satisfy the RoCoF relay requirement. In the practical scenario, the RoCoF relay contains a measuring window whose duration ranges from 40 ms to 2 s [48]. Notice that the RoCoF relay with a smaller time window is more sensitive and will identify a higher RoCoF value during a frequency event. Fig. 7 displays the reductions of the initial RoCoF with different t_s. To consider the worst situation, the RoCoF relay window length is selected as 50 ms in this article (the most sensitive one). It should be mentioned that the initial RoCoF is inversely proportional to the sum of $H_{\rm cap}$ and $H_{\rm M}$ [28]. In Fig. 7, the value of $H_{\rm M}$ is fixed and the increase of $H_{\rm cap}$ /$H_{\rm M}$ increases the total inertia and decreases the RoCoF.

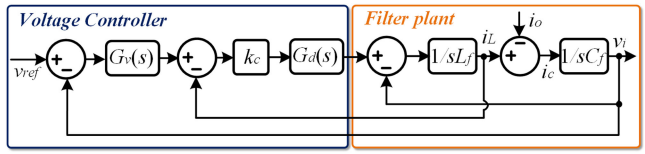

Fig. 8. Circuit and control block diagram of GCI.

If the synthetic inertia $H_{\rm cap}$ is ideally contributed by the GCI, the initial RoCoF is reduced by 1–$H_{\rm M}$ /($H_{\rm cap}$+$H_{\rm M}$) as compared with the situation when power system inertia is only contributed by $H_{\rm M}$ (mechanical inertia of the SM). When t_s is small enough, the reduction of the initial RoCoF is close to the ideal result since the dc capacitors of GCI can be quickly charged and discharged to provide the active power support. Nevertheless, as t_s increases, the initial RoCoF value cannot be reduced even with the synthetic inertia control. This is because dc capacitors cannot immediately response to for the compensation.

From Fig. 7, the value of t_s is selected as 0.2 s to effectively limit the initial RoCoF value. (Although t_s can be further smaller, stringent requirements will be imposed on inner-loop controller design, as will be discussed in the following section). From (40) and (42), the value of a_2 is given by

$$a_2 = a_0\left(\frac{\tau_s}{4.75}\right)^2 - \frac{C_{\rm dc}v_{\rm dc0}}{G_{eq}}. \tag{43}$$

Finally, the value of a_1 is confirmed as (to pursue $\xi = 1$)

$$a_1 = 2\left(\frac{a_0C_{\rm dc}v_{\rm dc0} + a_2a_0G_{eq}}{G_{eq}}\right)^{1/2}. \tag{44}$$

It should be mentioned that the knowledge of G_{eq} is required for the outer-loop parameter design. The value of R_g and L_g can be easily obtained from the impedance measurement approach in [49]. Note that the angle difference δ_0 is typically less than 5° such that G_{eq} can be approximated by assuming $1 \approx \cos\delta_0 >> \sin\delta_0$.

C. Inner-Loop Voltage Control Design

Previously, the transfer function $T(s)$ is derived and the outer-loop control parameters are determined. For simplification, the impact of inner-loop control is not considered. This assumption holds only if the bandwidth of inner-loop control is much higher than that of outer-loop control. For example, the value of ω_r is selected as 24 rad/s and the inner-loop bandwidth ω_b should be two decades larger. To fulfill this requirement, Fig. 8 shows the circuit and control block diagram of inner-loop voltage control. $G_v(s)$ is the voltage controller, k_c is the current regulation gain, and the system delay $G_d(s)$ equals

$$G_d(s) = e^{-1.5sT_s} \tag{45}$$

where T_s is the sampling frequency and $G_v(s)$ is given by

$$G_v(s) = \frac{k_p}{1 + s\tau} + \frac{k_r s}{s^2 + \omega_0^2} \tag{46}$$

where k_p is a proportional gain, τ is the time constant of a low-pass filter, and k_r is the resonant control gain. From Fig. 8, the

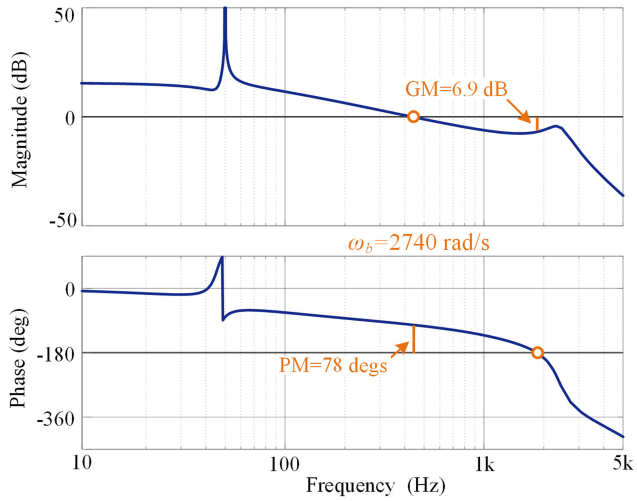

Fig. 9. Bode diagram of the designed $T_{in}(s)$.

TABLE I
SYSTEM PARAMETER VALUES

Inner-loop Control		
Parameters	Descriptions	Values
L_f	Filter inductance	0.5 mH
C_f	Filter capacitance	15 μF
T_s	Sampling period	50 μs
k_c	Current control gain	3
k_p	Proportional gain	2
k_r	Resonant gain	100
τ	Time constant	0.0025
Outer-loop Control		
Parameters	Descriptions	Values
C_{dc}	DC-link capacitance	1880 μF
ω_0	Nominal grid frequency	314 rad/s
v_{dc0}	Nominal DC-link voltage	200 V
V_0	Nominal GCI voltage magnitude	155 V
k_q	Reactive power droop gain	1×10^{-4} V/Var
a_0	Inertia control gain	0.05 rad/(s·V)
a_1	Control gain	4×10^{-3} rad/V
a_2	Control gain	5.2×10^{-5} rad/W
ω_r	Desired resonant frequency	24 rad/s
L_g	Feeder inductance	1 mH
R_g	Feeder resistance	0.5 Ω
G_{eq}	Equivalent gain	11000 W/rad

system open-loop transfer function is derived as

$$T_{in}(s) = \frac{G_v(s)k_cG_d(s)}{L_fC_fs^2 + k_cG_d(s)C_fs + 1}. \tag{47}$$

Fig. 9 displays the bode diagram of the designed $T_{in}(s)$, where all the parameters are provided in Table I. By properly selecting k_p, the control bandwidth is boosted to 2740 rad/s (436 Hz). In the meantime, the satisfied phase margin and gain margin can be realized through the tuning of τ (which neutralizes the influence of k_p in the high-frequency range) and k_c (which provides active damping against the LC resonance). Since ω_b is much larger than outer-loop resonant frequency ω_r. It is valid to decouple the dynamics of inner- and outer-loop controls.

TABLE II
POWER SYSTEM PARAMETERS

Parameters	Descriptions	Values
R	Frequency droop slope (p.u.)	0.05
T_G	Speed governor constant	0.1 s
F_{HP}	Turbine HP constant	0.3 s
T_{RH}	Reheater time constant	7.0 s
T_{CH}	Inlet volumes time constant	0.2 s
H_M	Inertia constant (p.u.)	3.5 s
t_d	RoCoF relay window length	50 ms
VA_{base}	System base power (1 p.u.)	500 VA

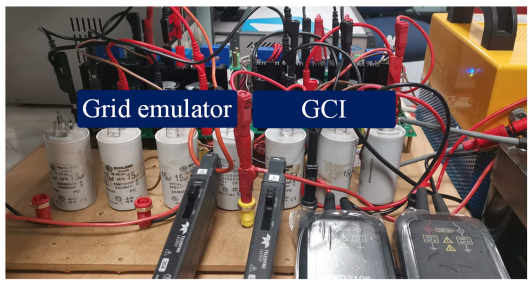

Fig. 10. Photo of the hardware setup.

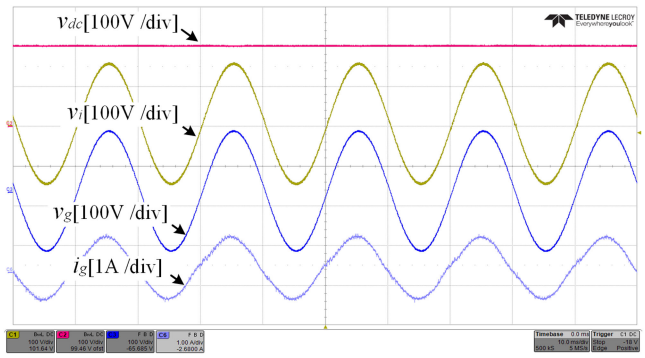

Fig. 11. Steady-state waveforms of dc-link voltages and grid currents.

V. EXPERIMENTAL RESULTS

To experimentally validate the performance of synthetic inertia control, a scaled-down power system prototype was built in the laboratory. The circuit control parameters are listed in Tables I and II and the circuit diagram is illustrated in Fig. 3(a). Fig. 10 shows the photo of the hardware setup, where the power system is emulated by an H-bridge dc–ac inverter and the GCI is connected with the grid emulator through feeder impedance.

A. Ideal Power Grid

Initially, the scenario of an ideal power grid is tested. Fig. 11 shows the steady-state waveforms when ω_g equals 314 rad/s. It can be observed that v_i is well synchronized with v_g and $v_{\rm dc}$ is regulated to be 200 V. Fig. 12 shows the responses when ω_g is intentionally changed from 314 rad/s to 313.5 rad/s. The step change of grid frequency can be quickly followed by the dc-link voltage. As observed in Fig. 12, the critical damping has been realized and the settling time is around 0.2 s. These agree

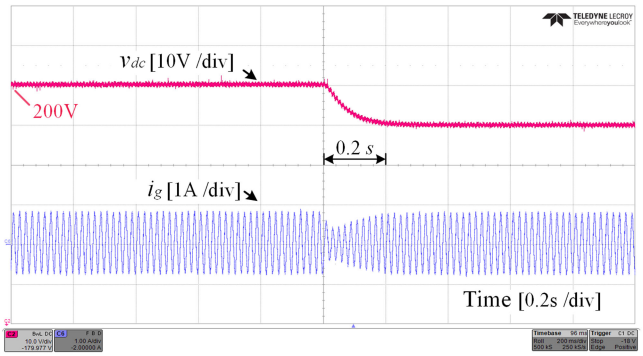

Fig. 12. Response of dc-link voltage and grid current after a step change of ω_g.

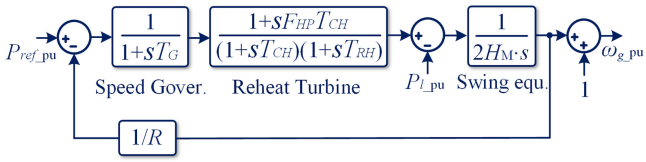

Fig. 13. Primary frequency regulation framework of the grid emulator.

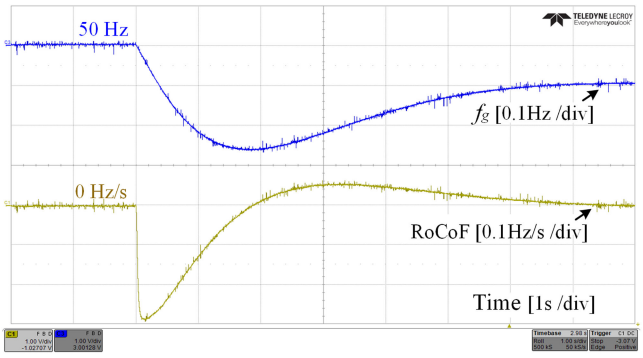

Fig. 14. Response of frequency and RoCoF without synthetic inertia control.

with the theoretical analysis and design result. Note that some second-order ripples exist in $v_{\rm dc}$, which can be reduced by [50].

B. Practical Power Grid

Then, the practical power grid is considered and the primary frequency regulation framework in Fig. 13 is incorporated into the frequency controller of the grid emulator. The RoCoF relay window length is 50 ms. Initially, the GCI is disconnected from the grid emulator. Fig. 14 shows the responses of grid frequency and RoCoF after a 4% power system step load change (through the change of R_L in Fig. 3). It can be observed that the measured instant RoCoF is as high as –0.28 Hz/s and the frequency nadir is 49.74 Hz.

Next, the GCI is connected with the grid emulator to provide synthetic inertia support and a 4% power system load change is similarly applied. Fig. 15 shows the responses of grid frequency and RoCoF with the designed control parameters. The synthetic inertia $H_{\rm cap}$ can be calculated by (8), which is around 2.36 s. As

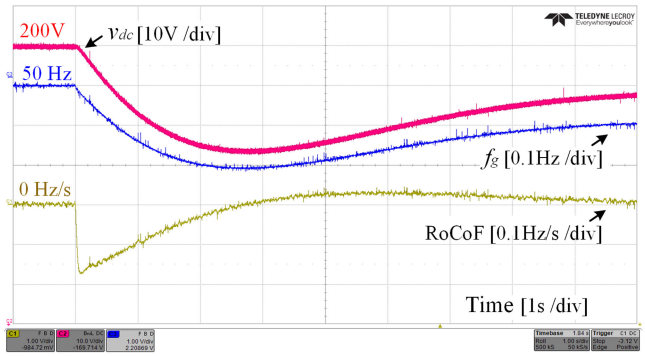

Fig. 15. Response of frequency and RoCoF with the synthetic inertia control.

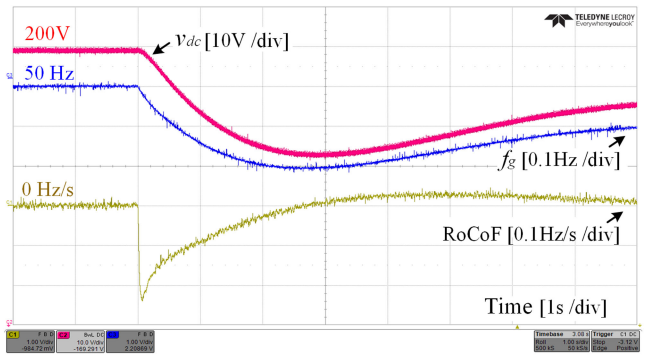

Fig. 16. Response of frequency and RoCoF with the sluggish inertia control.

shown in Fig. 15, the frequency nadir is increased to 49.8 Hz while the initial RoCoF is effectively reduced to –0.17 Hz/s. The result agrees well with the theoretical analysis, where the initial RoCoF is –0.28 Hz/s $\times$ $H_{\rm M}$ /($H_{\rm cap}$+$H_{\rm M}$) = –0.167 Hz/s. This indicates that the synthetic inertia is in close proximity to the physical inertia. In addition, the dc-link voltage can also track the grid frequency well.

Then, the value of a_1 is intentionally tuned as 1.2×10^{-2} rad/V such that $T(s)$ is overdamped with the sluggish synchronization dynamics. Fig. 16 displays the responses of grid frequency and RoCoF. Although the frequency nadir is equal to the previous result, the initial RoCoF value, which is –0.23 Hz/s, as shown in Fig. 16, cannot be limited as desired. This is due to the fact that dc-link capacitors cannot provide the active power support in a timely manner. In other words, the effect of synthetic inertia is different from that of the physical inertia at the beginning of a frequency event.

Next, the underdamped scenario has been tested by selecting a_1 as 1×10^{-3} rad/V and Fig. 17 shows the experimental result. Despite that the waveforms of the dc-link voltage and the grid frequency are comparatively smooth, the waveform of RoCoF suffers from poorly-damped oscillations. It can be observed that the maximum RoCoF value is about –0.22 Hz/s, which is worse than that of the critical-damping case (–0.17 Hz/s). Therefore, the underdamped scenario is less preferable as compared with the critical damping scenario.

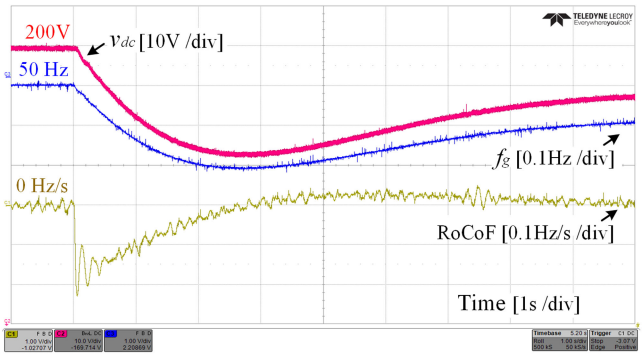

Fig. 17. Response of frequency and RoCoF with the oscillatory inertia control.

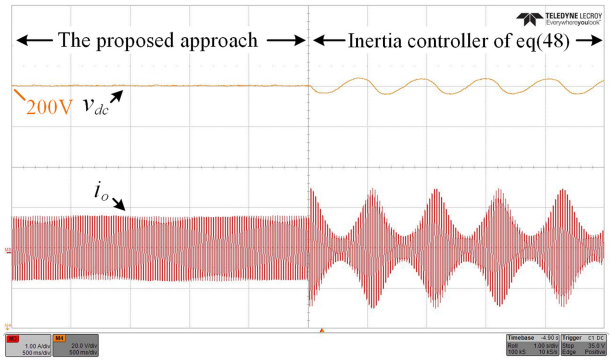

Fig. 18. Comparison between the proposed control and (48).

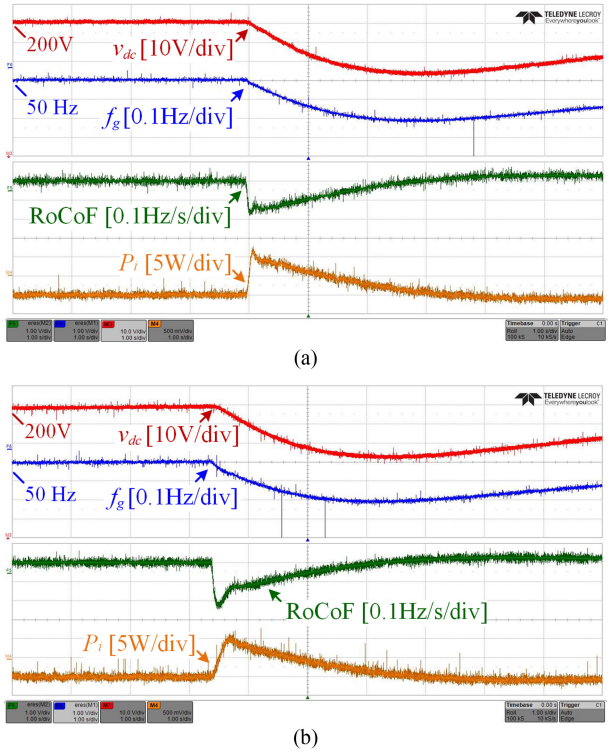

Fig. 19. Comparisons. (a) Proposed control. (b) $G_{AL}(s)$ given by (49).

C. Comparisons With Other Synthetic Inertia Control

An alternative approach to realize the synthetic inertia effect is to directly link the converter frequency f_i with the dc-link voltage $v_{\rm dc}$. The corresponding $G_{AL}(s)$ is given by

$$f_i = f_0 + \frac{1}{k}(v_{\rm dc} - v_{\rm dc\_ref}) \tag{48}$$

where f_0 is the nominal frequency. However, the direct implementation of (48) would result in undamped oscillations, as can be seen in Fig. 18. To solve this issue, a supplementary damping loop is needed. The detailed implementation is discussed in [39].

Besides, the analogy between the converter and synchronous machine can also be established by designing $G_{AL}(s)$ as

$$f_i = f_0 + \frac{s + K_T}{K_J s + K_D}(v_{\rm dc}^2 - v_{\rm dc\_ref}^2) \tag{49}$$

where K_J is the inertia coefficient, K_D is the damping coefficient, and K_T is the dc voltage tracking coefficient. Fig. 19 compares the proposed synthetic inertia control with the $G_{AL}(s)$ of (49). For a fair comparison, K_J is designed so that the dc capacitor provides the same amount of power to support grid frequency. In addition, K_D and K_T are designed such that the dc-link voltage is free from oscillations. It is observed that the initial RoCoF of Fig. 19(a) is smaller than that of Fig. 19(b). Moreover, the active power variation ΔP_i is strictly proportional to the grid RoCoF in Fig. 19(a). This agrees well with the math definition of inertia in (4).

VI. Conclusion

This article develops a synthetic inertia control with improved RoCoF suppression ability. The architecture of the developed controller is inversely determined to achieve a fast settling time with no undershoot/oscillation. In addition, an explicit step-by-step parameter design process has been provided. Experimental results of a scaled down power system prototype show that the proposed scheme can reduce the initial RoCoF by 40% and the frequency nadir by 23%.

References

[1] J. Fang, H. Li, Y. Tang, and F. Blaabjerg, "On the inertia of future more-electronics power systems," *IEEE J. Emerg. Sel. Topics Power Electron.*, vol. 7, no. 4, pp. 2130–2146, Dec. 2019.

[2] P. Kundur, *Power System Stability and Control*. New York, NY, USA: McGraw-Hill, 1994.

[3] Australian Energy Market Operator, "Black system South Australia, Sep. 28, 2016: final report," Mar. 2017.

[4] J. Driesen and K. Visscher, "Virtual synchronous generators," in *Proc. IEEE Power Energy Soc. Gen. Meeting*, Pittsburgh, PA, USA, 2008, pp. 1–3.

[5] H. Beck and R. Hesse, "Virtual synchronous machine," in *Proc. 9th Int. Conf. Electr. Power Qual. Utilisation*, Barcelona, Spain, 2007, pp. 1–6.

[6] Q. Zhong and G. Weiss, "Synchronverters: Inverters that mimic synchronous generators," *IEEE Trans. Ind. Electron.*, vol. 58, no. 4, pp. 1259–1267, Apr. 2011.

[7] Q. Zhong, P. Nguyen, Z. Ma, and W. Sheng, "Self-Synchronized synchronverters: Inverters without a dedicated synchronization unit," *IEEE Trans. Power Electron.*, vol. 29, no. 2, pp. 617–630, Feb. 2014.

[8] S. D'Arco and J. A. Suul, "Equivalence of virtual synchronous machines and frequency-droops for converter-based microgrids," *IEEE Trans. Smart Grid*, vol. 5, no. 1, pp. 394–395, Jan. 2014.

[9] D. Pan, X. Wang, F. Liu, and R. Shi, "Transient stability of voltage-source converters with grid-forming control: A design-oriented study," *IEEE J. Emerg. Sel. Topics Power Electron.*, vol. 8, no. 2, pp. 1019–1033, Jun. 2020.

[10] H. Wu *et al.*, "Small-signal modeling and parameters design for virtual synchronous generators," *IEEE Trans. Ind. Electron.*, vol. 63, no. 7, pp. 4292–4303, Jul. 2016.

[11] Z. Shuai, W. Huang, Z. J. Shen, A. Luo, and Z. Tian, "Active power oscillation and suppression techniques between two parallel synchronverters during load fluctuations," *IEEE Trans. Power Electron.*, vol. 35, no. 4, pp. 4127–4142, Apr. 2020.

[12] L. Huang, H. Xin, and Z. Wang, "Damping low-frequency oscillations through VSC-HVdc stations operated as virtual synchronous machines," *IEEE Trans. Power Electron.*, vol. 34, no. 6, pp. 5803–5818, Jun. 2019.

[13] J. Liu, Y. Miura, H. Bevrani, and T. Ise, "Enhanced virtual synchronous generator control for parallel inverters in microgrids," *IEEE Trans . Smart Grid*, vol. 8, no. 5, pp. 2268–2277, Sep. 2017.

[14] X. Hou, Y. Sun, X. Zhang, J. Lu, P. Wang, and J. M. Guerrero, "Improvement of frequency regulation in VSG-based AC microgrid via adaptive virtual inertia," *IEEE Trans. Power Electron.*, vol. 35, no. 2, pp. 1589–1602, Feb. 2020.

[15] A. Karimi *et al.*, "Inertia response improvement in AC microgrids: A fuzzy-based virtual synchronous generator control," *IEEE Trans. Power Electron.*, vol. 35, no. 4, pp. 4321–4331, Apr. 2020.

[16] W. Wu *et al.*, "Sequence impedance modeling and stability comparative analysis of voltage-controlled VSGs and current-controlled VSGs," *IEEE Trans. Ind. Electron.*, vol. 66, no. 8, pp. 6460–6472, Aug. 2019.

[17] X. Meng, J. Liu, and Z. Liu, "A generalized droop control for grid-supporting inverter based on comparison between traditional droop control and virtual synchronous generator control," *IEEE Trans. Power Electron.*, vol. 34, no. 6, pp. 5416–5438, Jun. 2019.

[18] T. Wen, D. Zhu, X. Zou, B. Jiang, L. Peng, and Y. Kang, "Power coupling mechanism analysis and improved decoupling control for virtual synchronous generator," *IEEE Trans. Power Electron.*, vol. 36, no. 3, pp. 3028–3041, Mar. 2021.

[19] J. Liu, Y. Miura, and T. Ise, "Comparison of dynamic characteristics between virtual synchronous generator and droop control in inverter-based distributed generators," *IEEE Trans. Power Electron.*, vol. 31, no. 5, pp. 3600–3611, May 2016.

[20] J. Fang, P. Lin, H. Li, Y. Yang, and Y. Tang, "An improved virtual inertia control for three-phase voltage source converters connected to a weak grid," *IEEE Trans. Power Electron.*, vol. 34, no. 9, pp. 8660–8670, Sep. 2019.

[21] Y. Hirase, K. Sugimoto, K. Sakimoto, and T. Ise, "Analysis of resonance in microgrids and effects of system frequency stabilization using a virtual synchronous generator," *IEEE J. Emerg. Sel. Topics Power Electron.*, vol. 4, no. 4, pp. 1287–1298, Dec. 2016.

[22] J. Morren, S.W. H. de Haan, W. L. Kling, and J. A. Ferreira, "Wind turbines emulating inertia and supporting primary frequency control," *IEEE Trans. Power Syst.*, vol. 21, no. 1, pp. 433–434, Feb. 2006.

[23] A. Mullane and M. O'Malley, "The inertial response of induction-machine-based wind turbines," *IEEE Trans. Power Syst.*, vol. 20, no. 3, pp. 1496–1503, Aug. 2005.

[24] Y. Qi, T. Yang, J. Fang, Y. Tang, K. R. R. Potti, and K. Rajashekara, "Grid inertia support enabled by smart loads," *IEEE Trans. Power Electron.*, vol. 36, no. 1, pp. 947–957, Jan. 2021.

[25] T. Chen, J. Guo, B. Chaudhuri, and S. Y. Hui, "Virtual inertia from smart loads," *IEEE Trans. Smart Grid*, vol. 11, no. 5, pp. 4311–4320, Sep. 2020.

[26] J. Zhu, J. M. Guerrero, W. Hung, C. D. Booth, and G. P. Adam, "Generic inertia emulation controller for multi-terminal voltage-source-converter high voltage direct current systems," *IET Renewable Power Gener.*, vol. 8, no. 7, pp. 740–748, Sep. 2014.

[27] J. Fang, H. Li, Y. Tang, and F. Blaabjerg, "Distributed power system virtual inertia implemented by grid-connected power converters," *IEEE Trans. Power Electron.*, vol. 33, no. 10, pp. 8488–8499, Oct. 2018.

[28] S. Yang, J. Fang, Y. Tang, H. Qiu, C. Dong, and P. Wang, "Modular multilevel converter synthetic inertia-based frequency support for medium-voltage microgrids," *IEEE Trans. Ind. Electron.*, vol. 66, no. 11, pp. 8992–9002, Nov. 2019.

[29] W. Wu *et al.*, "A virtual inertia control strategy for DC microgrids analogized with virtual synchronous machines," *IEEE Trans. Ind. Electron.*, vol. 64, no. 7, pp. 6005–6016, Jul. 2017.

[30] L. He, Y. Li, J. M. Guerrero, and Y. Cao, "A comprehensive inertial control strategy for hybrid AC/DC microgrid with distributed generations," *IEEE Trans. Smart Grid*, vol. 11, no. 2, pp. 1737–1747, Mar. 2020.

[31] J. Zhu, C. D. Booth, G. P. Adam, A. J. Roscoe, and C. G. Bright, "Inertia emulation control strategy for VSC-HVDC transmission systems," *IEEE Trans. Power Syst.*, vol. 28, no. 2, pp. 1277–1287, May 2013.

[32] Y. Phulpin, "Communication-free inertia and frequency control for wind generators connected by an HVDC-Link," *IEEE Trans. Power Syst.*, vol. 27, no. 2, pp. 1136–1137, May 2012.

[33] E. Waffenschmidt and R. S. Y. Hui, "Virtual inertia with PV inverters using DC-link capacitors," in *Proc. Eur. Conf. Power Electron. Appl.*, 2016, pp. 1–10.

[34] J. Khazaei, Z. Tu, and W. Liu, "Small-signal modeling and analysis of virtual inertia-based PV systems," *IEEE Trans. Energy Convers.*, vol. 35, no. 2, pp. 1129–1138, Jun. 2020.

[35] J. Fang, X. Li, and Y. Tang, "Grid-connected power converters with distributed virtual power system inertia," in *Proc. IEEE Energy Convers. Congr. Expo.*, Cincinnati, OH, USA, 2017, pp. 4267–4273.

[36] B. Wen, D. Dong, D. Boroyevich, R. Burgos, P. Mattavelli, and Z. Shen, "Impedance-based analysis of grid-synchronization stability for three-phase paralleled converters," *IEEE Trans. Power Electron.*, vol. 31, no. 1, pp. 26–38, Jan. 2016.

[37] Y. Huang, X. Yuan, J. Hu, and P. Zhou, "Modeling of VSC connected to weak grid for stability analysis of DC-link voltage control," *IEEE J. Emerg. Sel. Topics Power Electron.*, vol. 3, no. 4, pp. 1193–1204, Dec. 2015.

[38] J. Fang, X. Li, H. Li, and Y. Tang, "Stability improvement for three-phase grid-connected converters through impedance reshaping in quadrature-axis," *IEEE Trans. Power Electron.*, vol. 33, no. 10, pp. 8365–8375, Oct. 2018.

[39] S. A. Khajehoddin, M. Karimi-Ghartemani, and M. Ebrahimi, "Grid-supporting inverters with improved dynamics," *IEEE Trans. Ind. Electron.*, vol. 66, no. 5, pp. 3655–3667, May 2019.

[40] M. Ebrahimi, S. A. Khajehoddin, and M. Karimi-Ghartemani, "An improved damping method for virtual synchronous machines," *IEEE Trans. Sustain. Energy,* vol. 10, no. 3, pp. 1491–1500, Jul. 2019.

[41] L. Huang *et al.*, "A virtual synchronous control for voltage-source converters utilizing dynamics of DC-link capacitor to realize self-synchronization," *IEEE J. Emerg. Sel. Topics Power Electron.*, vol. 5, no. 4, pp. 1565–1577, Dec. 2017.

[42] D. Chen, Y. Xu, and A. Q. Huang, "Integration of DC microgrids as virtual synchronous machines into the AC grid," *IEEE Trans. Ind. Electron.*, vol. 64, no. 9, pp. 7455–7466, Sep. 2017.

[43] C. Arghir, T. Jouini, and F. Dörfler, "Grid-forming control for power converters based on matching of synchronous machines," *Automatica*, vol. 95, pp. 273–282, 2018.

[44] T. Wu, Z. Liu, J. Liu, S. Wang, and Z. You, "A unified virtual power decoupling method for droop-controlled parallel inverters in microgrids," *IEEE Trans. Power Electron.*, vol. 31, no. 8, pp. 5587–5603, Aug. 2016.

[45] Z. Chen, R. H. Lasseter, and T. M. Jahns, "Active power reserve control for grid-forming PV sources in microgrids using model-based maximum power point estimation," in *Proc. IEEE Energy Convers. Congr. Expo.*, 2019, pp. 41–48.

[46] Q. Peng, Y. Yang, T. Liu, and F. Blaabjerg, "Coordination of virtual inertia control and frequency damping in PV systems for optimal frequency support," *CPSS Trans. Power Electron. Appl.*, vol. 5, no. 4, pp. 305–316, Dec. 2020.

[47] J. Fang, R. Zhang, H. Li, and Y. Tang, "Frequency derivative-based inertia enhancement by grid-connected power converters with a frequency-locked-loop," *IEEE Trans. Smart Grid*, vol. 10, no. 5, pp. 4918–4927, Sep. 2019.

[48] V. Knap, S. K. Chaudhary, D. Stroe, M. Swierczynski, B. Craciun, and R. Teodorescu, "Sizing of an energy storage system for grid inertial response and primary frequency reserve," *IEEE Trans. Power Syst.*, vol. 31, no. 5, pp. 3447–3456, Sep. 2016.

[49] J. C. Vasquez, J. M. Guerrero, A. Luna, P. Rodriguez, and R. Teodorescu, "Adaptive droop control applied to voltage-source inverters operating in grid-connected and islanded modes," *IEEE Trans. Ind. Electron.*, vol. 56, no. 10, pp. 4088–4096, Oct. 2009.

[50] L. Zhang and X. Ruan, "Control schemes for reducing second harmonic current in two-stage single-phase converter: An overview from DC-bus port-impedance characteristics," *IEEE Trans. Power Electron.*, vol. 34, no. 10, pp. 10341–10358, Oct. 2019.

Yang Qi (Member, IEEE) received the B.Sc. degree from Xi'an Jiaotong University, Xi'an, China, in 2016, and the Ph.D. degree from Nanyang Technological University, Singapore, in 2021, both in electrical engineering.

He was a Visiting Student with Power Electronics, Microgrids, and Subsea Electrical Systems Center, in 2019. Since 2021, he has been with the School of Automation, Northwestern Polytechnical University as an Associate Professor. His research interests include modeling and control of power-electronics-based power systems.

Dr. Qi was the recipient of the Doctoral Research Excellence Award from Nanyang Technological University, in 2021.

Han Deng (Graduate Student Member, IEEE) received the B.Eng. degree in electrical engineering from Xi'an Jiaotong University, Xi'an, China, in 2017, and the M.Sc. degree in power engineering in 2018 from Nanyang Technological University, Singapore, where she is currently working toward the Ph.D. degree.

Her research interests include modeling, stability analysis, and control of distributed generation in more-electronics power systems.

Xiong Liu (Senior Member, IEEE) received the B.E. and M.Sc. degrees in electrical engineering from the Huazhong University of Science and Technology, Wuhan, China, in 2006 and 2008, respectively, and the Ph.D. degree from the School of Electrical and Electronic Engineering, Nanyang Technological University, Singapore, in 2013.

From July to November 2008, he was an Engineer with Shenzhen Nanrui Technologies Company, Ltd., Shenzhen, China. From September 2011 to January 2012, he was a Visiting Scholar with the Department of Energy Technology, Aalborg University, Aalborg East, Denmark. From April 2012 to December 2013, he was a Researcher with Energy Research Institute, Nanyang Technological University. From December 2013 to July 2020, he was working as a Principal Technologist with Rolls-Royce Electrical, Rolls-Royce Singapore Pte. Ltd., Singapore. He is currently an Associate Professor with Energy Electricity Research Center, International Energy College, Jinan University, Zhuhai, China. His research interests include power electronics, motor drive, and electrical/hybrid propulsion system for marine and aerospace.

Yi Tang (Senior Member, IEEE) received the B.Eng. degree in electrical engineering from Wuhan University, Wuhan, China, in 2007, and the M.Sc. and Ph.D. degrees from the School of Electrical and Electronic Engineering, Nanyang Technological University, Singapore, in 2008 and 2011, respectively.

From 2011 to 2013, he was a Senior Application Engineer with Infineon Technologies Asia Pacific, Singapore. From 2013 to 2015, he was a Postdoctoral Research Fellow with Aalborg University, Aalborg, Denmark. Since March 2015, he has been with Nanyang Technological University, where he is currently an Associate Professor. He is the Cluster Director of the Advanced Power Electronics Research Program with the Energy Research Institute, Nanyang Technological University.

Dr. Tang was a recipient of the Infineon Top Inventor Award in 2012, the Early Career Teaching Excellence Award in 2017, the Best Associate Editor Award for IEEE JOUNRAL OF EMERGING AND SELECTED TOPICS IN POWER ELECTRONICS in 2018, the Outstanding Reviewer for the IEEE TRANSACTIONS ON POWER ELECTRONICS in 2019, and four IEEE Prize Paper Awards. He is an Associate Editor for the IEEE TRANSACTIONS ON POWER ELECTRONICS and the IEEE JOUNRAL OF EMERGING AND SELECTED TOPICS IN POWER ELECTRONICS.